Digest Journal of Nanomaterials and Biostructures Vol. 18, No. 4, October-December 2023, p.1293-1303

Microstructure and crystallographic texture of direct energy deposition printed 316L stainless steel

H. R. Zhi[a], H. T. Zhao[a,*], Y. F. Zhang[b], B. Dampilon[b]
[a]*School of Materials Science and Engineering, Shenyang Ligong University, Shenyang, China*
[b]*Shenyang Jinfeng special equipment Co. Ltd, Shenyang, China*

The microstructural features and crystallographic texture of 316L stainless steel prepared by direct energy deposition (DED) are studied. The grain size, morphology, grain boundary, misorientation distribution along different direction and mechanical properties are characterized via detailed electron backscatter diffraction (EBSD) analysis and Vickers microhardness tester. The DED-built 316L stainless steel exhibits equiaxed cellular and elongated morphology. Only a few number of dislocations are accumulated and entangled near small grain boundary. The sample contains mainly large angle grain boundary. 316L stainless steel powder is melted to form a deep and shallow shape measured from the top view. The average grain size is 38.32 μm and 29.79 μm for the top and side view, respectively. Two strong textural components of {001}<100> cube texture and {110}<001> Goss texture are formed perpendicular and parallel to the scanning direction, respectively. The microhardness of DED-built 316L stainless steel achieves a higher average value of 261.74 HV.

(Received August 29, 2023; Accepted October 20, 2023)

Keywords: Additive manufacturing, Direct energy deposition, 316L stainless steel, Microstructure, Microhardness.

1. Introduction

Additive manufacturing (AM) technology has been widely used in industry [1-4], particularly for fabricating complex metal parts with excellent mechanical properties [5]. AM can print multiple materials, such as Ti-based, Al-based, Mg-based, Cu-based and Fe-based alloys [6-17].

Among the various materials, 316L stainless steel is very popular for producing metallic parts by means of AM. Austenitic 316L stainless steel (SS) is attractive alloy for engineers and scientists due to their superior properties such as high mechanical strength and excellent corrosion [18-21]. A lot of efforts have been made to improve the 316L SS for additive manufacturing [22-29].

Powder-based additive manufacturing techniques are generally divided into two broad categories, namely directed energy deposition (DED) and selective laser melting (SLM). SLM is a

* Corresponding author: zht95711@163.com
https://doi.org/10.15251/DJNB.2023.184.1293

popular method for producing metallic parts, and it has commercially available production facilities [30,31]. While DED is a recently developed technology that has not been much explored. In the process, the raw material in the form of powder or wire is inserted directly into the molten pool produced by the laser and subsequently deposited layer by layer [32]. The DED method can produce complex parts with near-net shape or to handle damaged or worn areas of components [33].

So far, there have been few reports in the literature of austenitic steels manufactured by DED technology. Much of this research has focused on the effects of process parameters or heat treatment on the microstructure and mechanical properties of DED 316L [34]. However, the impact of the printing direction on the microstructure and crystal texture of the DED prepared samples is still minimal. Therefore, the aim of this present work is to study microstructural characteristics and texture by analyzing the grain size, morphology and misorientation distribution in different directions of DED prepared samples through detailed EBSD analysis. Furthermore, Vickers microhardness is tested. Therefore, the results of the study can help to provide factual evidence for future applications of 316 L stainless steel manufactured by DED.

2. Materials and methods

2.1. Sample preparation

The powder particles are 316 L stainless steel prepared by gas atomization. The composition of the powder is all values in wt. %: Fe 66.11, Cr 16.0, Mn 13.0, Mo 3.3, Si 0.9, C 0.07 and N 0.62. Fig. 1 shows the morphology and size distribution of gas atomized powder particles. The powder particles are approximately spherical in shape and have a symmetrical size distribution. The average diameter is around 57.04 μm (d10 =39.41 μm, d50 = 63.28μm, d90 = 90.69 μm).

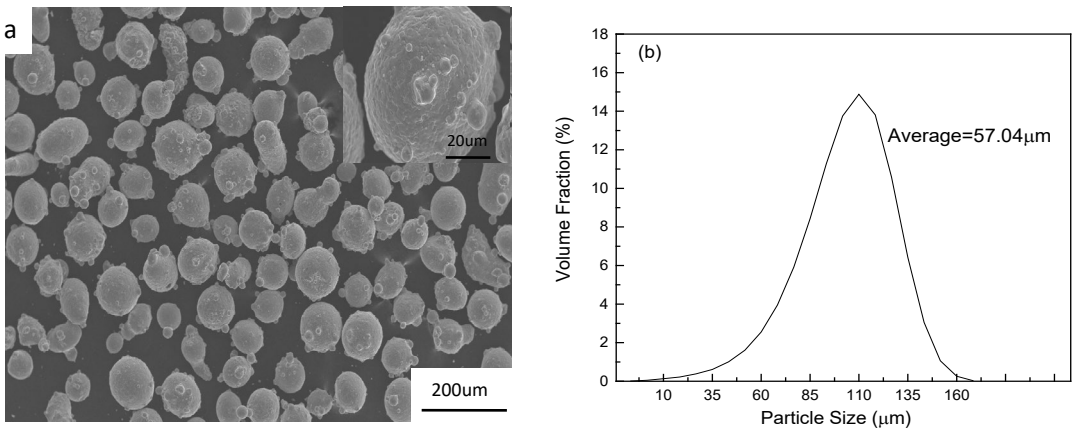

Fig. 1. Particle size distribution of powder.

The samples are printed on a 304 substrate using the JF-M2000R coaxial powder feeding 3D printer. The device is equipped with a single fiber laser that prints in an argon atmosphere by scanning layer by layer along the X axis. The main printed parameters are as follows: laser power, scanning speed, spot size, hatch spacing of 400 W, 10 mm/s, 50 μm and 0.5 mm, respectively.

2.2. Microstructure characterization and mechanical testing

The grain size and morphology, texture and crystal phases for the DED-built 316L stainless steel were obtained by EBSD experiments. The accelerating voltage and beam current for the EBSD testing were 20 kV and 3 nA, respectively. The analysis of the data was performed via Oxford HKL Channel 5 software. The average microhardness of 5 trials for the DED-built 316L samples from the side view were measured using a Vickers hardness tester at a load of 300 g for 10 s.

3. Results and discussion

Representative three-dimensional view of the DED-built microstructure is presented in Fig. 2a. The SEM examination of micrographs does not show the evidence of cracks, pores or un-melted powder. Fig. 2b displays the inverse pole figures (IPF) of the DED-built 316 L stainless steel specimens. It shows random growth of particle color and epitaxial growth of grains arranged in the direction of the maximum temperature gradient from the remelting region. As seen from the front view, elongated grains are developed along the Z direction. The elongated grains mostly grow across the melt-pool boundaries continuously along building direction[35].

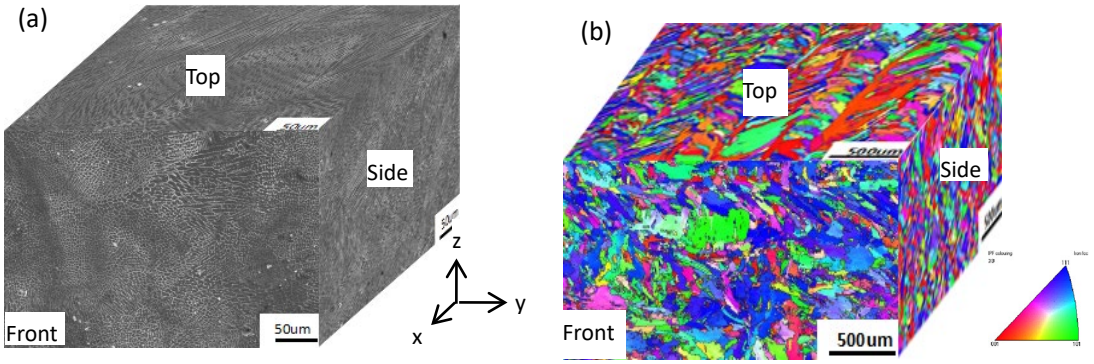

Fig. 2. Three-dimensional view of the DED-built micrograph (a) and inverse pole figure map (b)

Fig. 3 shows SEM photos of the typical unit cell micromorphology. It can be observed from Fig. 3a that the sample contains equiaxed cellular and elongated morphology. Fig.3a shows that homogeneous cellular substructure are equiaxed and its size is uniform with about 5–6 μm in diameter. The elongated cells generally observed along the molten pool boundary, as shown in Fig. 3b-c. The elongated cells are often impeded at the solidification front, forming a new grain with random crystallographic orientation[36]. The cellular morphology is often caused by rapid cooling rates and thermal gradients during the printing process. It is observed that the solidification microstructure can evolve from unidirectional to equiaxed to dendritic with faster cooling rate[37].

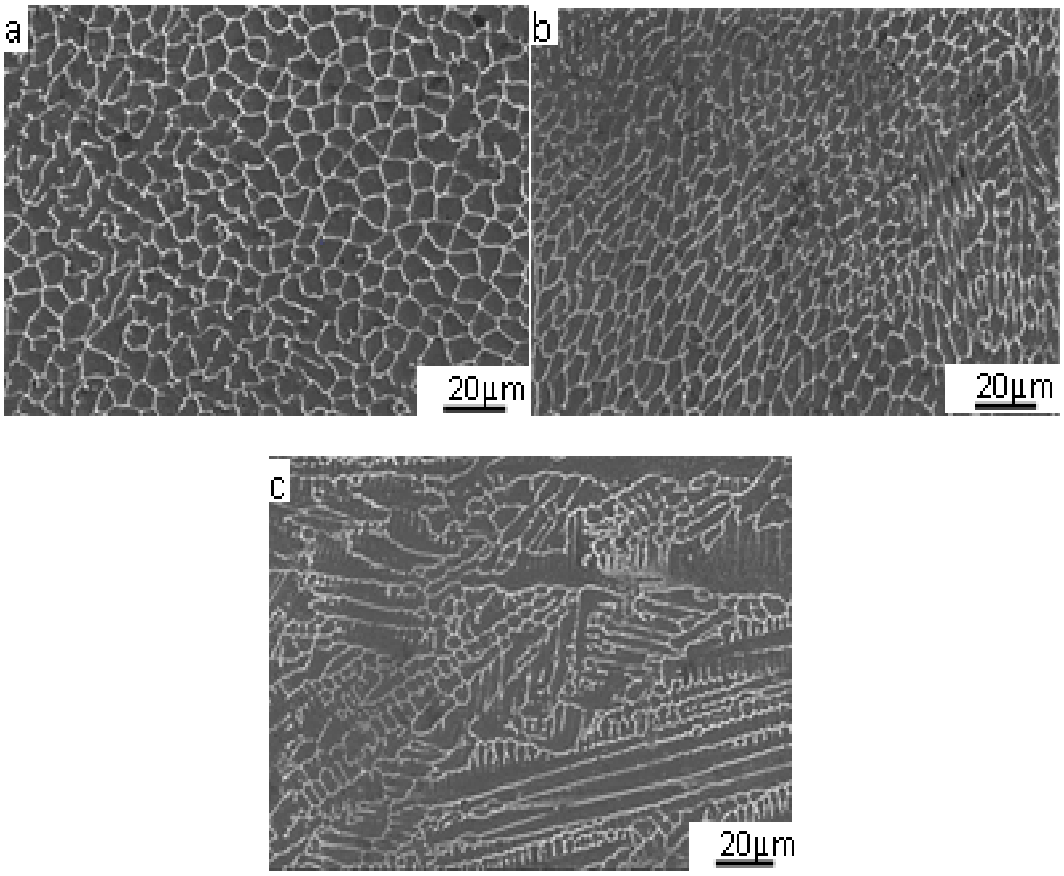

Fig. 3. SEM images of the DED-built 316L stainless steel.

Microstructures and textures of the DED-built 316L stainless steel measured from the top view is presented in Fig. 4. The Kernel average misorientation (KAM) diagram, also known as local misorientation diagram, is used to describe the deformation degree of material grains. The green lines in KAM diagram can be approximately regarded as dislocations, which are caused by lattice distortion with large deformation. Only a few dislocations can be seen accumulating and entangled near the small grain boundaries (as shown in Fig. 4a). This implies no higher residual stress within this sample. Fig. 4b shows the grain boundary and misorientation spread map. The black and green lines represent the large angle grain boundary (the orientation difference is more than 15 °) and small angle grain boundary (orientation difference between 2° and 15°), respectively. It can be observed that the sample contains mainly large angle grain boundary, which provides obstacles to cleavage crack propagation [38,39] and thus enhance the fracture toughness. The grain size varies from about 19 to 184 μm with average grain size of 38.32 μm (as shown in Fig. 4c). In terms of the textures, it exhibits a typical {001}<100> cube texture, with texture intensity of 4.79 (Fig. 4e).

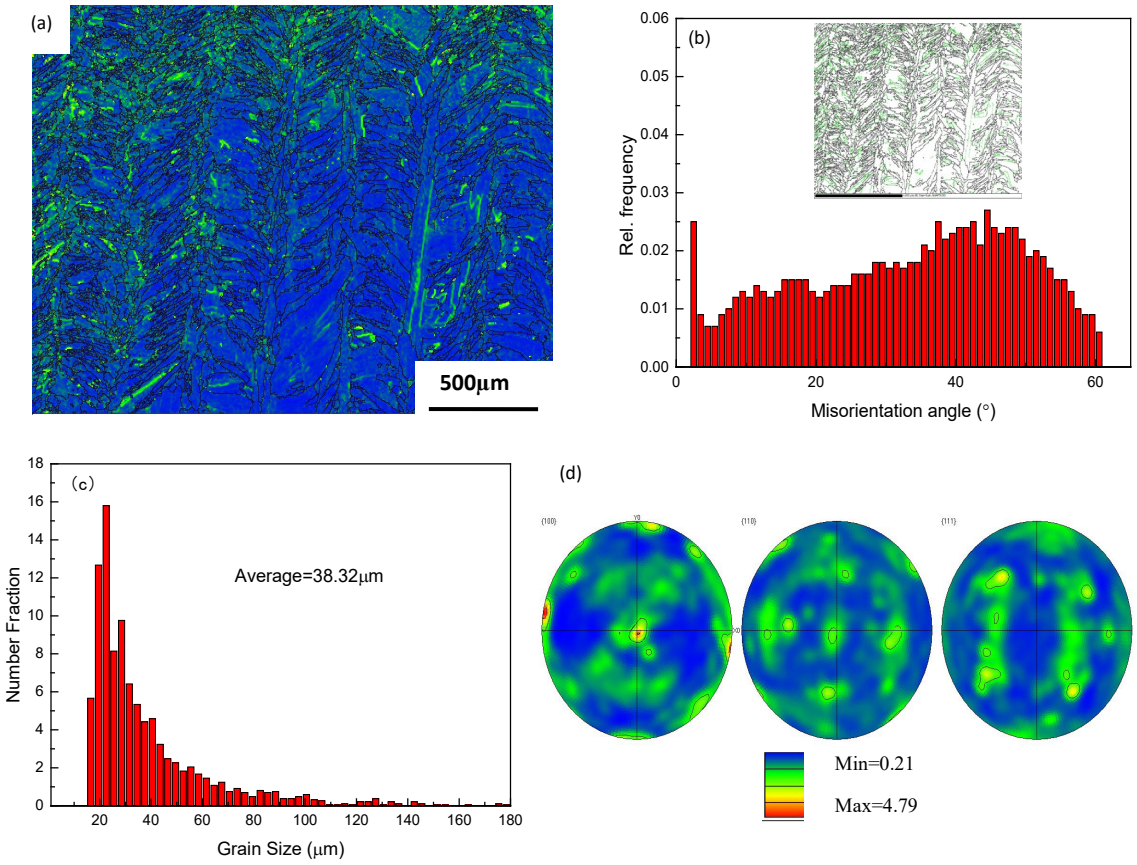

Fig.4 Microstructures and textures of the DED-built 316L stainless steel measured from the top view. (a) KAM map. (b)grain boundary and grain orientation spread map. (c) grain size distribution. (d) pole figures.

Fig. 5a shows inverse pole figure map measured from the top view. The centers of laser scan tracks and edges of melt pool are marked by white and black dotted lines, respectively, which help understand the grain growth behavior during the melt pool solidification[40]. It is observed that the hatch spacing is about 500 μm. Grains can be observed growing from the boundary towards the center of the molten pool, and the grains at the boundary are finer. 316L stainless steel powder is melted to form a shallow shape. Fig. 5b indicates the finer grains with size less than 30μm are seen near the melt-pool boundaries and center. These finer grains are oriented in random direction, thus created no texture preference (as shown in Fig. 5c).

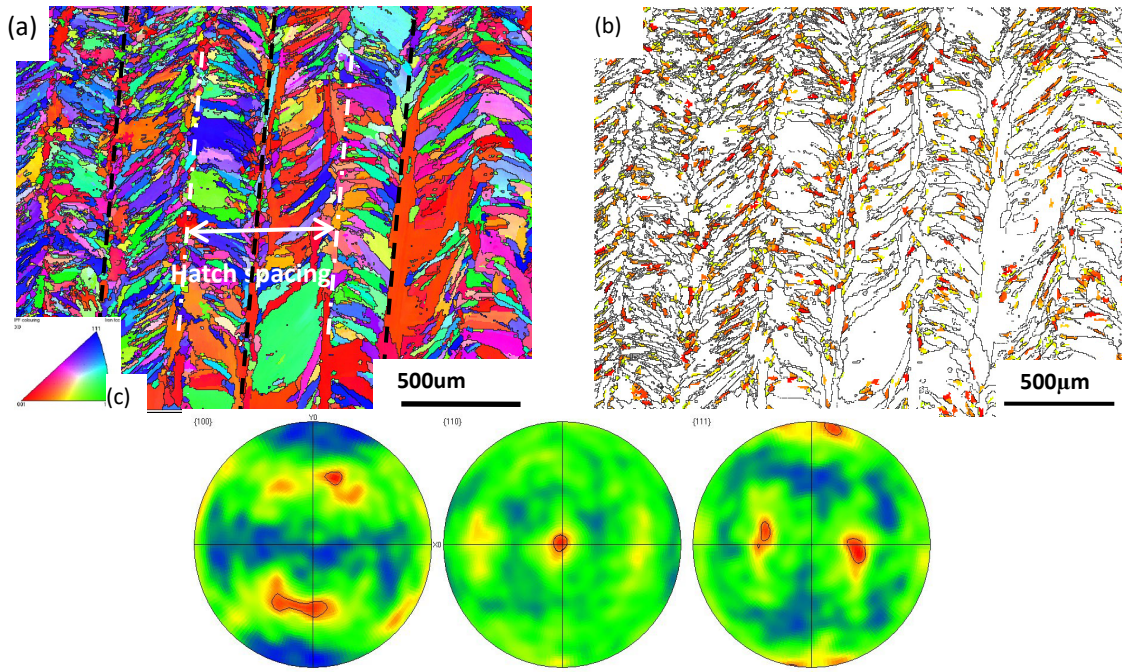

Fig. 5. The grains and morphology of the DED-built 316L stainless steel measured from the top view. (a) Inverse pole figure map. (b) Inverse pole figure map of grains with size less than 30μm and (c) correspondingpole figure map.

In order to quantitatively study the evolution of crystal orientation in the grains, Fig.6 b-c show the orientation difference analysis along the indicator line in Fig.6 a. As shown in Fig.6 b-c, the crystal orientation in the grain changes unobviously. The orientation difference (red line) of point to point is less than 1°, and the orientation difference (black line) of a point relative to the origin point is almost close to 3°. This phenomenon means that the subgrain rotation is unobvious.

Fig.7 shows microstructures and textures of the DED-built 316L stainless steel measured from the side view. IPF map reveals that the microstructure is composed of two different size grains with a uniform grain distribution (as shown in Fig. 7a). The grain size varies from about 12.48 to 156.08 μm with average value of 29.79 μm (as shown in Fig. 7b). The formation of coarse grains is due to the use of high heat input energy density which resulted in an annealing effect and grain growth in the subsequent DED process[41]. Fig.7c shows the red markers are finer grains smaller than 30 μm in size, with fine grains surrounding the coarse grains. The grain size in the same alloy varies from fine grains to coarse grains, reflecting the local changes in thermal history due to the overlaps of adjacent melt pool during DED process[42]. The mechanism of texture evolution depends on the interplay between the direction of maximum thermal gradient and preference for an epitaxial growth across the deposited layers[43]. The texture consists of a strong {110}<001 > Goss texture and a weak {111}<112> annealed texture with a texture intensity of 3.90 (Fig. 6d). In the cubic system, the <001> is the building direction, which is consistent with the thermal gradient direction and is also conducive to the grain growth direction.

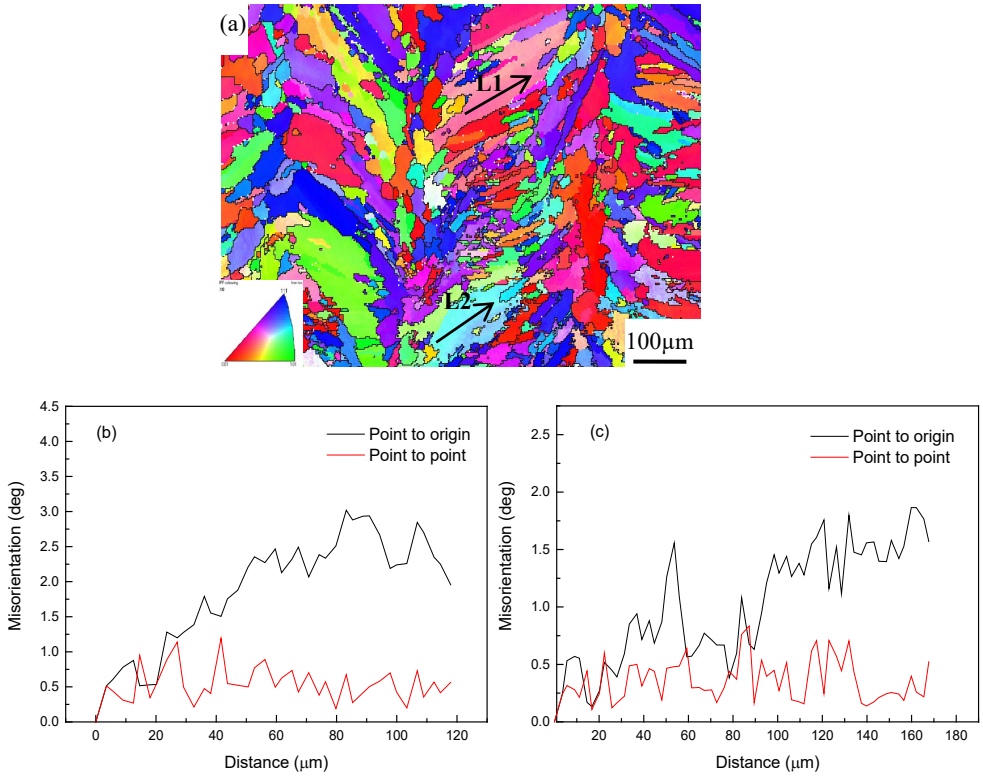

Fig. 6(a) IPF map of the DED-built 316L stainless steel for the top view. (b,c) the misorientations measured along the arrows marked L1 and L2, respectively.

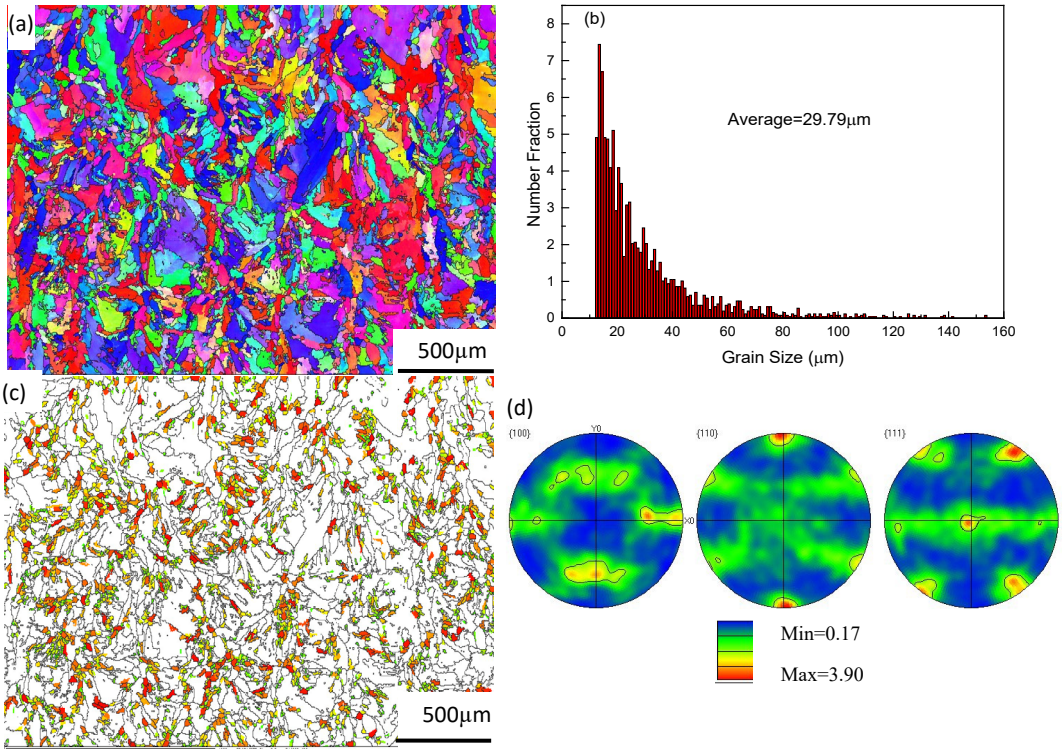

Fig.7 Microstructures and textures of the DED-built 316L stainless steel measured from the side view. inverse pole figure map.(b) grain size distribution.(c) inverse pole figure map of grains with size less than 30μm.(d) pole figure.

Fig. 8a shows IPF map including melt pool and substrate from the side view. In the case of the IPF map, the molten pool pattern is represented by the white dotted curves along the boundary. The molten pool has an uneven microstructure of rough and fine grains because of the high heat input and steep thermal gradients around the molten pool. Particles can be observed to grow epitaxially from the boundary along the building direction to the center of the molten pool, which is due to solidification growth in the direction of the center of the molten pool. This growth method reduces the nucleation barrier of the penultimate layer during solidification. The width of the melt pool is approximately 500μm. The morphology of the heat affected zone (HAZ) between the molten pool and the substrate of the printed sample consists of very fine martensitic particles of the substrate. This is due to a very large thermal gradient and rapid cooling during the DED process. EBSD phase map shows the austenite face centered cubic (FCC) grains are formed during DED process, and the substrate is made of martensitic body centered cubic (BCC) fine grains with average grain size of about 9 μm (as shown in Fig.8b).

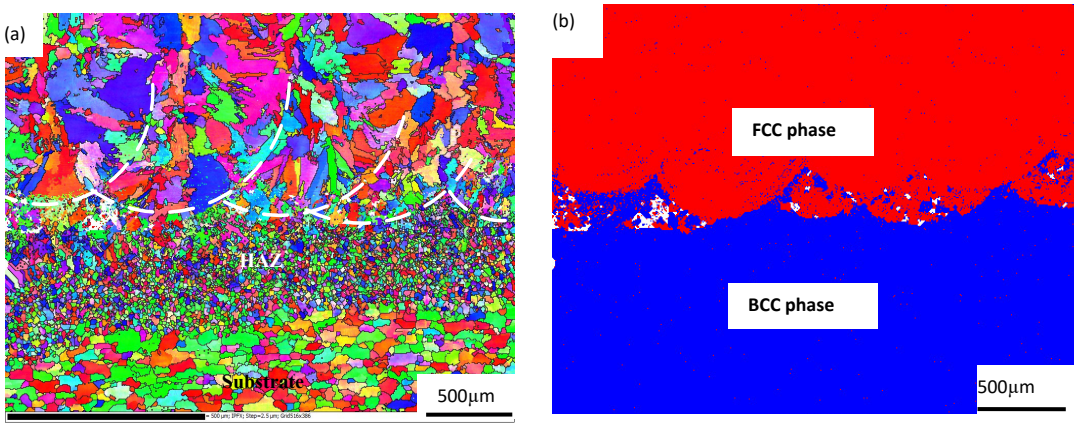

Fig. 8 (a) Inverse pole figure map and (b) Phase map including the melt pool and substrate from the side view.

Fig. 9 shows the microhardness distribution across the different microstructural zones for DED-built specimen from the side view. As can be seen from the figure, the substrate has a lower microhardness value. The hardness of the heat affected zone increases significantly, due to the relatively fine grain size of the heat affected zone. The microhardness value is high within printed 316Lstainless steel, and the corresponding average values is 261.74 HV. The combination effect of grain orientation and texture component results in higher hardness in the DED-built 316L stainless steel. Laser additive stainless steel blocks are overlapped in multiple layers along the building direction. The first printed layer passes through this position again during or after solidification, and the next layer of stainless steel continues to be formed on this basis. Due to the change of thermal gradient, the morphology distribution within and between the printing layers is not very uniform. Therefore, the hardness value fluctuates slightly along the building direction, but it is relatively homogeneous on the whole.

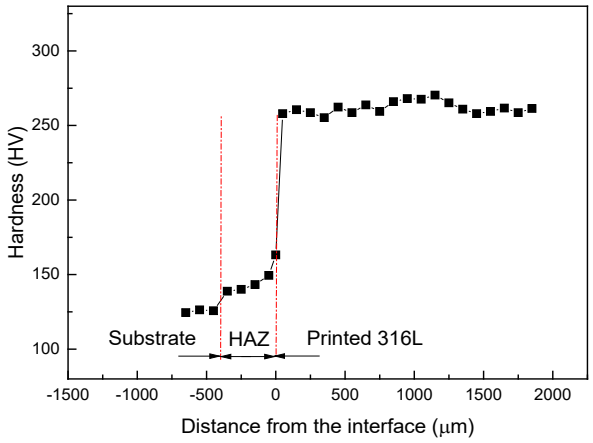

Fig. 9. Microhardness distribution of the DED-built 316L stainless steel measured from the side view.

4. Conclusions

The sample contains equiaxed cellular and elongated morphology. Only a few number of dislocations are accumulated and entangled near big grain boundary, which implies no higher residual stress within the printed sample. The sample contains mainly large angle grain boundary, which provides obstacles to cleavage crack propagation and thus enhance the fracture toughness. The finer grains with size less than 30μm are seen along the melt-pool boundaries and center for the top view. The grain size varies from about 12.48 to 156.08 μm with average value of 29.79 μm measured from the side view. The subgrain rotation is not obvious. The molten pool has an uneven microstructure of rough and fine grains because of the high heat input and big thermal gradients around the molten pool. The width of the molten pool is approximately 500μm. The microhardness value is high within printed 316Lstainless steel, and the corresponding average value is 261.74 HV. The hardness value fluctuates slightly along the building direction, but it is relatively homogeneous on the whole.

Acknowledgments

This study was funded by Planned Project of Department of Science and Technology of Liaoning Province (2023JH2/10700022).

References

[1] J. Wang, W. Wu, W. Jing, X. Tan, G. Bi, Mater Sci Eng A, 746, 300 (2019); https://doi.org/10.1016/j.msea.2019.01.019

[2] G. Zeng, T. Song, Y. Dai, H. Tan, M. Yan, Mater Design, 169, 107693 (2019); https://doi.org/10.1016/j.matdes.2019.107693

[3] A.T. Sidambe, Y. Tian, P.B. Prangnell, P. Fox, Inter J Refr Met Hard Mater, 78, 254 (2019);

https://doi.org/10.1016/j.ijrmhm.2018.10.004

[4] T. Ching, Y. Li, R. Karyappa, A. Ohno, Sens Actua: B. Chem, 297, 126609 (2019); https://doi.org/10.1016/j.snb.2019.05.086

[5] S. Zun, X. Tan, M. Descoins, D. Mangelinck, S.B. Tor, C.S. Lim, Scripta Mater, 168, 129 (2019); https://doi.org/10.1016/j.scriptamat.2019.04.036

[6] C. Shang, C. Wang, C. Li, G. Yang, G. Xu, Optic Lase Technol, 126, 106100 (2020); https://doi.org/10.1016/j.optlastec.2020.106100

[7] L. Chen, J. Huang, C. Lin, C. Pa, S. Chen, Mater Sci Eng A, 682, 389 (2016); https://doi.org/10.1016/j.msea.2016.11.061

[8] S. Barui, A. Panda, S. Naskar, R. Kuppuraj, S. Bas, Biomater, 213, 119212 (2019); https://doi.org/10.1016/j.biomaterials.2019.05.023

[9] Y. Zhang, Z. Chen , S. Qu, A. Feng, G. Mi, J Alloys Comp, 825, 153971 (2020); https://doi.org/10.1016/j.jallcom.2020.153971

[10] Y. Zhou, W. Li, L. Zhang, S. Zhou, X. Jia, J Mater Process Technol, 276, 116398 (2020); https://doi.org/10.1016/j.jmatprotec.2019.116398

[11] J. Wang, M. Zhang, X. Tan, T. Liu, G. Bi, Mater Sci Eng A, 777, 139049 (2020); https://doi.org/10.1016/j.msea.2020.139049

[12]M. Salehi, S. Maleksaeedi, S.M. Nai, G.K. Meenashisundaram, M. Gupta, Add. Manuf, 29, 100790 (2019); https://doi.org/10.1016/j.addma.2019.100790

[13] M. Salehi, S. Maleksaeedi, S.M. Nai, G.K. Meenashisundaram, Acta Mater, 165, 294 (2019); https://doi.org/10.1016/j.actamat.2018.11.061

[14] Z. Liu, W. Zhou, Y. Lu, H. Xu, Z. Qin, Mater Lett, 225, 85 (2018); https://doi.org/10.1016/j.matlet.2018.04.114

[15] G. Ma, Z. Li, L. Wang, Constr Build Mater, 162, 613 (2018); https://doi.org/10.1016/j.conbuildmat.2017.12.051

[16] S. Gurminder, M.P. Pulak, J Manuf Proce, 43, 253 (2019); https://doi.org/10.1016/j.jmapro.2019.05.010

[17] L. Kučerová, I. Zetková, A. Jandová, M. Bystrianský, Mater Sci Eng A, 750, 70 (2019); https://doi.org/10.1016/j.msea.2019.02.041

[18] D. Kong, C. Dong, X. Ni, L. Zhang, Corro Sci, 166, 108425.1 (2020); https://doi.org/10.1016/j.corsci.2019.108425

[19] J. Zhang, L. Qin, F. Liu, C. Lou, Dig J Nanomater Bios, 17(4), 1151(2022); https://doi.org/10.15251/DJNB.2022.173.1151

[20] A.M. Roach, B.C. White, A. Garland, B.H. Jared, Add. Manuf, 32, 101090 (2020); https://doi.org/10.1016/j.addma.2020.101090

[21] F.C. Pinto, I.R. Filho, M.J. Sandi, H.R. Sandim, Add. Manuf, 31, 100979 (2020); https://doi.org/10.1016/j.addma.2019.100979

[22] Z. Zhang, B. Chu, L. Wang, Z. Lu, J Alloy Comp, 791, 166 (2019); https://doi.org/10.1016/j.jallcom.2019.03.082

[23] M. Song, M. Wang, X. Lou, R.B. Rebak, G.S. Was, J Nucl Mater, 513, 33 (2019); https://doi.org/10.1016/j.jnucmat.2018.10.044

[24] Y. Hong, C. Zhou, Y. Zheng, L, Zhang, J. Zheng, Mater Sci Eng A, 740, 420 (2019);

https://doi.org/10.1016/j.msea.2018.10.121

[25] J.M. Jeon, J.M. Park, J.H. Yu, J.G. Kim, Y.J. Seong, Mater Sci Eng A, 763, 138152 (2019); https://doi.org/10.1016/j.msea.2019.138152

[26] M.S.Phama, B. Dovgyy, P.A. Hooper, Mater Sci Eng A, 704, 102 (2017); https://doi.org/10.1016/j.msea.2017.07.082

[27] B. Li, B. Qian, Y. Xu, Z. Liu, J. Zhang, Mater Sci Eng A, 745, 495 (2019); https://doi.org/10.1016/j.msea.2019.01.008

[28] J.C. Simmons, X.B. Chen, A. Azizi, M.A. Daeumer, P.Y. Zavalij, Add. Manuf, 32, 100996 (2020); https://doi.org/10.1016/j.addma.2019.100996

[29] D. Gu, H. Chen, Mater Sci Eng A, 725, 419 (2018); https://doi.org/10.1016/j.msea.2018.04.046

[30] A. Rai, H. Helmer, C. Körner, Add. Manuf, 13, 124 (2016); https://doi.org/10.1016/j.addma.2016.10.007

[31] J.A. Koepf, M.R. Gotterbarm, M. Markl, C. Körner, Acta Mater, 152, 119 (2018); https://doi.org/10.1016/j.actamat.2018.04.030

[32] B. Bax, R. Rajput, R. Kellet, M. Reisacher, Add. Manuf, 21, 487 (2018); https://doi.org/10.1016/j.addma.2018.04.002

[33] K.S. Prakash, T. Nancharaih, V.V. Rao, Mater Today Proc, 5, 3873 (2018); https://doi.org/10.1016/j.matpr.2017.11.642

[34] B. Barkia, P. Aubry, P. Haghi-Ashtiani, T. Auger, L. Gosmain, J Mater Sci Technol, 41, 209 (2020); https://doi.org/10.1016/j.jmst.2019.09.017

[36] J.M. Jeon, J.M. Park, J.H. Yu, J.G. Kim, Y.J. Seong, S.H. Park, H.S. Kim, Mater Sci Eng A, 763, 138152 (2019); https://doi.org/10.1016/j.msea.2019.138152

[37] B. Li, L. Zhang, Y. Xu, Z. Liu, B. Qian, F. Xuan, Powder Technol, 360, 509 (2020); https://doi.org/10.1016/j.powtec.2019.10.068

[38] J.F. Lancaster, Elsevier, (1999).

[39] J. Nohava, P. Hausild, M. Karlik, P. Bompard, Mater Charact, 49, 211 (2002); https://doi.org/10.1016/S1044-5803(02)00360-1

[40] A.F. Gourgues, H.M. Flower, T.C. Lindley, Mater Sci Technol, 16, 26 (2000); https://doi.org/10.1179/026708300773002636

[41] C.H. Hung, A. Sutton, Y.Q. Li, Y.Y. Shen, J Manuf Proces, 45, 438 (2019); https://doi.org/10.1016/j.jmapro.2019.07.030

[42] D.K. Kim, W. Woo, E.Y. Kim, S.H. Choi, J Alloys Comp, 774, 896 (2019; https://doi.org/10.1016/j.jallcom.2018.09.390

[43] Q. Tan, J. Zhang, N. Mo, Z. Fan, Y. Yin, Add Manuf, 32, 101034 (2020); https://doi.org/10.1016/j.addma.2019.101034

[44] S. Bahl, S. Mishra, K.U. Yazar, I.R. Kola, K. Chatterjee, Add Manuf, 28, 65 (2019); https://doi.org/10.1016/j.addma.2019.04.016